

## FULL ARTICLE

# Step-by-step monitoring of a magnetic and SERS-active immunosensor assembly for purification and detection of tau protein

Viktor Maurer<sup>1,2,3,4</sup> | Claudia Frank<sup>4</sup> | Julian Cedric Porsiel<sup>1,4</sup> |  
Sabrina Zellmer<sup>1,5</sup> | Georg Garnweitner<sup>1,2,3\*</sup>  | Rainer Stosch<sup>3,4</sup>

<sup>1</sup>Institute for Particle Technology (iPAT), Technische Universität Braunschweig, Braunschweig, Germany

<sup>2</sup>Center of Pharmaceutical Engineering (PVZ), Technische Universität Braunschweig, Braunschweig, Germany

<sup>3</sup>Laboratory for Emerging Nanometrology (LENA), Technische Universität Braunschweig, Braunschweig, Germany

<sup>4</sup>Physikalisch-Technische Bundesanstalt (PTB), Braunschweig, Germany

<sup>5</sup>Fraunhofer Institute for Surface Engineering and Thin Films (IST), Braunschweig, Germany

## \*Correspondence

Georg Garnweitner, Institute for Particle Technology (iPAT), Technische Universität Braunschweig, Volkroder Str. 5, 38104, Braunschweig, Germany.  
Email: g.garnweitner@tu-bs.de

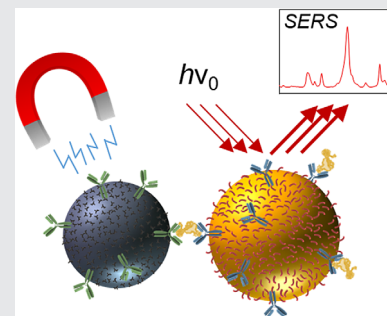
## Funding information

EMPIR, Grant/Award Number: 15HLT02

## Abstract

We report a bottom-up synthesis of iron oxide and gold nanoparticles, which are functionalized and combined to form a nanohybrid serving as an immune sensor, which selectively binds to tau protein, a biomarker for diagnosis of

Alzheimer's disease. Detection of the target analyte is achieved by surface-enhanced Raman scattering originating from the diagnostic part of the nanohybrid that was prepared from Au nanoparticles functionalized with 5,5'-dithiobis-(2-nitrobenzoic acid) as a Raman reporter and monoclonal anti-tau antibody. The magnetic part consists of Fe<sub>x</sub>O<sub>y</sub> nanoparticles functionalized with polyclonal anti-tau antibody and is capable to separate tau protein from a complex matrix such as cerebrospinal fluid. We further identified and validated a set of analytical tools that allow monitoring the success of both nanoparticle preparation and each functionalization step performed during the assembly of the two binding sites by an immune reaction. By applying UV/Vis spectroscopy, dynamic light scattering, zeta potential measurements, X-ray diffraction, small-angle X-ray scattering, and transmission electron microscopy, we demonstrate a proof-of-concept for a controlled and step-by-step traceable synthesis of a tau protein-specific immune sensor.



**Abbreviations:** AD, Alzheimer's disease; CSF, cerebrospinal fluid; DLS, dynamic light scattering; DTNB, 5,5'-dithiobis-(2-nitrobenzoic acid); EA, elemental analysis; EDC, 1-ethyl-3-(3-dimethyl-aminopropyl)carbodiimide; Fe<sub>x</sub>O<sub>y</sub>, iron oxide; HEPES, 4-(2-hydroxyethyl)-1-piperazineethanesulfonic acid; IVDs, in-vitro diagnostic devices; NHS, N-hydroxysuccinimide; NP(s), nanoparticle(s); PEG, polyethylene glycol; SAXS, small-angle X-ray scattering; SERS, surface-enhanced Raman scattering; SI, international system of units; TEM, transmission electron microscopy; TGA, thermogravimetric analysis; TNB, 5-thio-2-nitrobenzoic acid; XRD, X-ray diffraction.

This is an open access article under the terms of the Creative Commons Attribution-NonCommercial License, which permits use, distribution and reproduction in any medium, provided the original work is properly cited and is not used for commercial purposes.

© 2019 The Authors. *Journal of Biophotonics* published by WILEY-VCH Verlag GmbH & Co. KGaA, Weinheim

**KEYWORDS**

hybrid nanoparticles, Immunosensor, SERS, tau protein

**1 | INTRODUCTION**

Over the last 15 years, nanoparticles (NPs) have found numerous applications in biotechnology and medicine [1–4]. For example, the plasmonic properties of noble metal NPs are used for imaging applications such as Raman spectroscopy to investigate molecules, pathogens, and tissues [5–7]. In cases where the target analyte does not provide a sufficient Raman signal, plasmonic materials such as gold (Au) NPs can enhance the Raman-cross sections of the adsorbed molecules, known as surface-enhanced Raman spectroscopy (SERS) [8]. If the target analyte does not directly interact with plasmonic NPs or does not itself provide a significant SERS spectrum, so-called SERS tags may instead serve as sensitive analytical probes. A SERS tag consists of plasmonic NPs and a Raman-active reporter molecule on the NP surface having binding sites selective toward the target analyte. Successful binding of the analyte is then detected indirectly through the Raman signature of the reporter [9, 10]. Using suitable conjugation techniques, SERS tags can be further modified to provide additional functionalities, for example, through coupling of Au NPs to magnetic components such as iron oxide ( $\text{Fe}_x\text{O}_y$ ) NPs. In this way, sensitive detection resulting from the plasmonic surface can be effectively combined with the ability for magnetic separation of the analyte from complex matrices [11, 12].

The ability of a SERS assay to magnetically capture the target analyte and separate it from potentially interfering matrix compounds is particularly important for the detection of disease-specific biomarkers in body fluids such as cerebrospinal fluid (CSF). Several approaches to build up multicomponent SERS assays have been proposed for the identification and quantification of biomarkers such as enzymes [13], mRNA [14, 15], or viral DNA [16]. A good overview of SERS-based immunoassays has been recently presented by Lai et al [17]. The high sensitivity of the SERS tag makes this method a promising approach for the detection and monitoring of diseases associated with exceptionally low biomarker concentrations. This applies, for example, to tau protein which is considered as one of the most important biomarkers for Alzheimer's disease (AD) [18, 19]. Zengin et al. established such a multicomponent SERS tag for the quantification of tau protein with a limit of detection below 25 fmol/L [20].

In clinical chemistry and laboratory medicine, those markers are typically measured with the help of in vitro diagnostic devices (IVDs). Often a quality assurance of

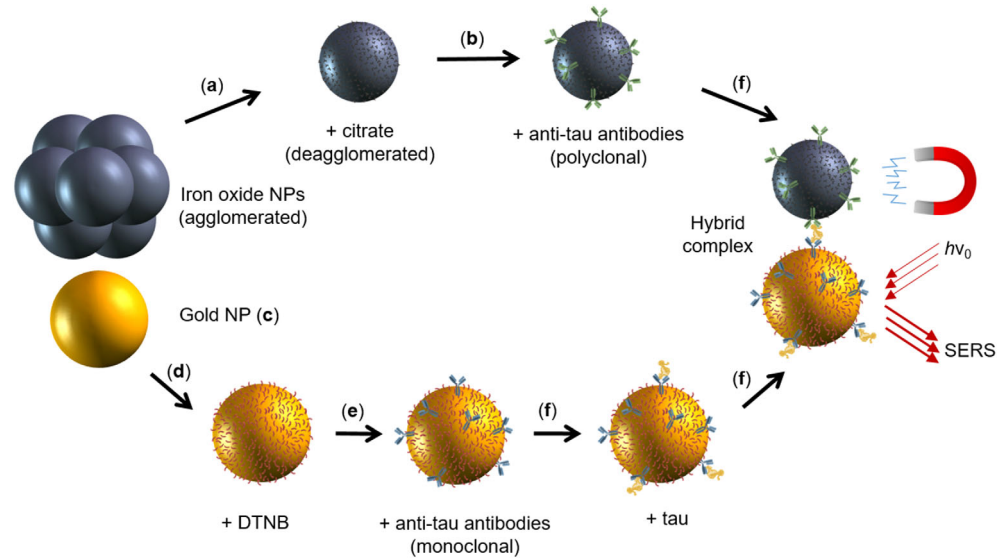
such routine analyses is required by law [21]. For this purpose, so-called reference measurement methods must be provided, which are ideally connected directly to the international system of units (SI) [21–23]. It has already been demonstrated that SERS-based methods are basically suitable for realizing the required SI-traceability [24, 25]. However, the establishment of a reference measurement method to quantify extremely low concentrations of large biomarker molecules such as tau protein is still challenging and time consuming. One of the reasons is that metrological validation requires the measurement result being associated with a measurement uncertainty. However, a reliable estimation of the uncertainty budget according to internationally accepted guidelines is only possible if the underlying process is fully understood and traceable [26].

Here, we present a defined route for the assembly of the entire SERS assay with a focus on monitoring each individual step of the preparation (Figure 1). In comparison to the system of Zengin *et al.* [20], a simplification of the magnetic component significantly reduced the synthesis duration and workload for preparation of the whole tau protein-specific immunosensor. The proposed approach can also be transferred to other protein biomarkers by exchanging the specific antibody. After functionalizing Au NPs with 5,5'-dithiobis-(2-nitrobenzoic acid) (DTNB), the  $\text{Fe}_x\text{O}_y$ - and Au NPs were modified with polyclonal and monoclonal anti-tau antibodies, respectively. Finally, the complete SERS tag is formed by coupling of the two NP entities through the tau protein. The preparation of the particles as well as each step of the hybrid system formation were characterized by several methods, such as dynamic light scattering (DLS), elemental analysis (EA), small-angle X-ray scattering (SAXS), transmission electron microscopy (TEM), thermogravimetric analysis (TGA), UV/Vis spectroscopy, X-ray diffraction (XRD), and zeta potential measurements.

**2 | MATERIALS AND METHODS/  
EXPERIMENTAL****2.1 | Chemicals and reagents**

The antibodies (monoclonal and polyclonal SP70 anti-tau antibody, both produced in rabbit), 1-ethyl-3-(3-dimethylaminopropyl)carbodiimide (EDC,  $\geq 98\%$ ), gold(III) chloride (99%), 4-(2-hydroxyethyl)-1-piperazineethanesulfonic acid

**FIGURE 1** Schematic depiction of the hybrid complex formation with the individual experimental steps tagged and described below



(HEPES,  $\geq 99.5\%$ ), hydrochloric acid (37%), sodium-(L) ascorbate ( $\geq 98\%$ ), N-hydroxysuccinimide (NHS,  $\geq 98\%$ ), sodium hydroxide (NaOH,  $\geq 97\%$ ), polyethylene glycol 600 (PEG, techn. grade) and tau protein (Tau-411 human expressed in *E. coli*,  $\geq 90\%$ ) were obtained from Sigma-Aldrich Chemie GmbH (Taufkirchen, Germany). DTNB ( $\geq 99\%$ ) was acquired from AppliChem GmbH (Darmstadt, Germany). Absolute ethanol (EtOH, 99.5%) was supplied by Fisher Scientific GmbH (Schwerte, Germany). Sodium citrate dihydrate ( $\geq 99.95\%$ ) was purchased from Honeywell Fluka (Seelze, Germany). Acetone (techn. grade) was obtained from VWR International GmbH (Darmstadt, Germany). The  $\text{Fe}_x\text{O}_y$  NPs were purchased as a powder from IoLiTec Inc. (Heilbronn, Germany). All chemicals were used as received.

To minimize the standard uncertainties of the concentrations, all solutions were handled gravimetrically. Unless otherwise stated, ultrapure water (18 M $\Omega$ -cm) was used, which was prepared from pre-cleaned tap water using a Millipore Elix 5 UV device in combination with a Milli-Q Element A10. The HEPES buffer was prepared by dissolving 0.063 g of HEPES powder in 50 g of ultrapure water and adjusting to a pH of 7.48–7.52 using a 0.1 mol/L NaOH solution.

## 2.2 | Preparation of citrate-modified iron oxide nanoparticles (a)

For the magnetic component, 0.17 g of  $\text{Fe}_x\text{O}_y$  powder was dispersed in 50 mL of sodium citrate solution (0.018 mol/L) and mixed in a 50 mL of stainless steel container with 54.3 g of 200  $\mu\text{m}$  zirconia grindings [27]. After 1 hour at 400 rpm in a planetary ball mill (PM400, Retsch GmbH), the suspension color turned black. Subsequent filtration of the solution through a 50  $\mu\text{m}$  mesh separates the grinding

media and after centrifugation at 1000 g for 5 minutes, sedimented bigger aggregates were removed from the solution and the supernatant with the remaining particles was mixed with acetone (5:1 v/v acetone/supernatant). The precipitated particles were centrifuged at 2400 g for 5 minutes and resuspended in ultrapure water after discarding the supernatant. This washing procedure was repeated for two more times. The resulting concentration of  $\text{Fe}_x\text{O}_y$  NP was about 3 mg/mL, as determined by quantification with phenanthroline [28]. For further experiments, this solution was diluted with HEPES buffer in a ratio of 1:8 (v/v) and centrifuged at 10000 g for 10 minutes. After magnetic separation on a magnetic rack (MagRack 6, GE Healthcare), the supernatant was exchanged with HEPES buffer. Centrifugation and buffer exchange were performed twice.

## 2.3 | Immobilization of anti-tau antibodies on iron oxide nanoparticles (b)

To couple anti-tau antibodies to the citrate modified  $\text{Fe}_x\text{O}_y$  NPs, 14  $\mu\text{L}$  of an aqueous EDC solution (1.92 mg/mL) and 2  $\mu\text{L}$  of an NHS solution (1.15 mg/mL) were added quickly one by one to 1 mL of  $\text{Fe}_x\text{O}_y$  NP solution. After incubation for 12 minutes, 2  $\mu\text{L}$  of polyclonal anti-tau antibodies were added, mixed carefully, and incubated at room temperature for 3 hours. Afterward, the particles were centrifuged for 20 minutes at 2000 g and after magnetic separation the supernatant was replaced with HEPES buffer, which was repeated twice.

## 2.4 | Synthesis of gold nanoparticles (c)

The synthesis of Au NPs was carried out analogously to the patent of Taniuchi *et al.* [29] with some

modifications. For the nucleation step (core colloid), gold-(III) chloride (0.17 g) was dissolved in 25 mL of ultrapure water and sodium citrate dihydrate (0.49 g) was dissolved in 100 mL of ultrapure water. Six milliliters of the gold chloride solution ( $4.1 \cdot 10^{-4}$  mol/L) were diluted in 200 mL of ultrapure water, refluxed with heating in a PEG bath and stirred (ca. 700 rpm) for 30 minutes. After reaching a constant temperature of about 100°C, 50 mL of citric acid solution ( $1.6 \cdot 10^{-4}$  mol/L) was added, refluxed with heating, and stirred for another 15 minutes. Afterward, the Au NPs were cooled down to room temperature. For the synthesis of the final colloid, 233 mL each of a gold-(III) chloride solution ( $1.7 \cdot 10^{-4}$  mol/L) and a sodium-(L) ascorbate solution ( $4.7 \cdot 10^{-4}$  mol/L) were added (volumetric flow rate = 2 mL/min using a calibrated peristaltic pump) to 12 mL of the solution of core colloid ( $3 \cdot 10^{-4}$  mol/L, previously heated to 30°C) and stirred at 700 rpm. After complete addition of the precursors, the final solution was kept at 30°C for 1 hour, followed by centrifuging the particles (core colloids at 17000 g for 30 minutes, final colloids at 2000 g for 20 minutes) and replacing the supernatant with HEPES buffer (adjusted to optical density (OD) 1).

## 2.5 | DTNB functionalization of gold nanoparticles (d)

Ten microliters of DTNB solution (10 mmol/kg in EtOH) were added to 1 mL Au NP dispersion. After 15 minutes incubation, the suspension was centrifuged for 20 minutes at 2000 g and the supernatant was replaced with HEPES buffer. The purification step was performed twice.

## 2.6 | Immobilization of anti-tau antibodies on DTNB-functionalized gold nanoparticles (SERS tag) (e)

Two microliters of monoclonal anti-tau antibody solution were added to a suspension of 1 mL DTNB-functionalized Au NPs, which was incubated for 3 hours at room temperature. Afterward, the particles were washed with HEPES buffer by centrifuging the solution at 2000 g for 20 minutes and exchanging the supernatant for two times.

## 2.7 | Capturing of tau protein with the SERS tag and separation with magnetic nanoparticles (f)

Two microliters of tau protein solution (1  $\mu\text{g}/\mu\text{L}$  in ultrapure water) were added to 1 mL of the surface-

modified Au NPs and incubated at room temperature for 3 hours. Then, 1 mL of surface-modified  $\text{Fe}_x\text{O}_y$  NPs were added and incubated over night at room temperature. The subsequent purification was a two-fold centrifugation at 1000 g for 10 minutes, wherein a magnetic purification was carried out using a MagRack 6 for approximately 30 minutes. After the second washing step, the hybrid complex was diluted in 200  $\mu\text{L}$  of HEPES buffer.

## 2.8 | Characterization methods

DLS and zeta potential measurements were performed with a Zetasizer Nano from Malvern Instruments. For DLS, all samples were diluted by a factor of  $10^4$ – $10^5$  to minimize occurring fluorescence and then measured three times with a 173° backscattering set-up. Data evaluation was accomplished using the Zetasizer Nano software whereby the volume distributions were utilized for the assessment of hydrodynamic diameters. Zeta potentials were measured using a capillary zeta cuvette (DTS1070C, Malvern Panalytical Ltd).

EA was carried out with a FlashEA 1112 from Thermo Quest after drying the samples under vacuum conditions.

SAXS was performed with a SAXSess mc<sup>2</sup> from Anton Paar utilizing Cu- $K_\alpha$  radiation (wavelength: 0.154 nm, voltage: 50 mA, current: 40 kV) and a CCD detector. At room temperature, a 1 mm flow-through quartz cuvette was used at a sample-to-detector distance of 309 mm. Exposure times were between 0.1 and 100 seconds and the measuring times between 2 and 1000 seconds. The sample was measured in transmission mode with a slit collimation setup. The scattering data were routinely corrected [30] with respect to the background, transmission, instrumental noise, and smearing effects from the slit collimated beam. Basic steps were done in SAXSquant (Anton Paar GmbH, Austria), whereas desmearing and the indirect Fourier transformation (IFT) were carried out in GIFT (PCG software package, University Graz) [31]. The IFT translates the scattered information into real space and yields a model-free pair distance distribution function ( $P[r]$ ), visualizing all frequencies of lengths between individual scatters within the system. The relatively most occurring distance is observable by the mode of the  $P(r)$ , which equals the radius ( $R_{\text{max}}$ ) for spherical particles.

SERS spectra were acquired using a LabRAM Aramis Raman microscope and LabSpec 5 Software from Horiba Jobin-Yvon. The instrument was equipped with a 1200 grooves/mm holographic grating and a HeNe excitation laser (633 nm). For sample preparation, 200  $\mu\text{L}$  of the nanohybrid solution were incubated on a silanized

microscope slide overnight and were then air dried. Each sample was irradiated with an exposure time of  $200 \cdot 1$  seconds. The spot size was  $\sim 550$  nm. The spectra were accumulated and measured three times each. Calibration of the spectral line position was carried out prior to each acquisition using the polystyrene ring breathing mode at  $1001.4 \text{ cm}^{-1}$ , according to the recommendations given in the ASTM guideline [32].

TEM images were taken with a Tecnai G<sup>2</sup> F20 TMP from Fei at 200 kV. The samples were applied onto a carbon film on a 3.05 mm woven copper net with 300 mesh from Plano GmbH.

TGA was performed using a TGA/DSC 1 STARE system and a gas controller 4C200 STARE system from Mettler Toledo. Fifteen milligrams of the dried sample were put in a ceramic crucible and measured at a heating rate of  $10^\circ\text{C}/\text{min}$  under an oxygen atmosphere.

UV/Vis spectra were recorded using a LAMBDA 1050 dual-beam photometer from Perkin Elmer, measuring in a Quartz Suprasil semi-micro cuvette (layer thickness 1.0 cm) from Hellma Analytics.

XRD was carried out with an Empyrean device from Panalytical. The measurements were carried out with  $\text{Cu-K}\alpha$  radiation (wavelength  $\lambda$  of 0.154 nm) on a Si sample holder in a range of  $2\theta$  from  $20$  to  $90^\circ$  and a step size of  $0.05^\circ$ .

### 3 | RESULTS AND DISCUSSION

#### 3.1 | Preparation of the magnetic component

After the dispersion process in the planetary ball mill, TEM images show  $\text{Fe}_x\text{O}_y$  NPs with sizes between 18 and 24 nm and divergent morphologies (Figure 2A). By increasing the focus, TEM images displaying the lattice fringes of the crystalline  $\text{Fe}_x\text{O}_y$  NPs could be obtained (Figure S1A). DLS measurements revealed a hydrodynamic diameter of approximately 24.7 nm with a polydispersity index (PDI) around 0.3 (Figure 2B). The tailing of the DLS curves toward larger particle sizes hints to the presence of some agglomerates, which is a classic result of top down processes since mechanical energy acts arbitrarily [33]. A subsequent immobilization of anti-tau resulted in an increase of the hydrodynamic diameter by approximately 10 nm (Figure 2B), about twice as much as was detected for other types of immunoglobulin G (IgG) with similar molar weight [34], indicating multiple binding on single  $\text{Fe}_x\text{O}_y$  NPs. UV/Vis measurements show an increase of the OD (Figure S1B) in the specific absorbance region of IgGs (approximately 250–280 nm, [35]) after adding anti-tau, which is most likely based on successful antibody immobilization.

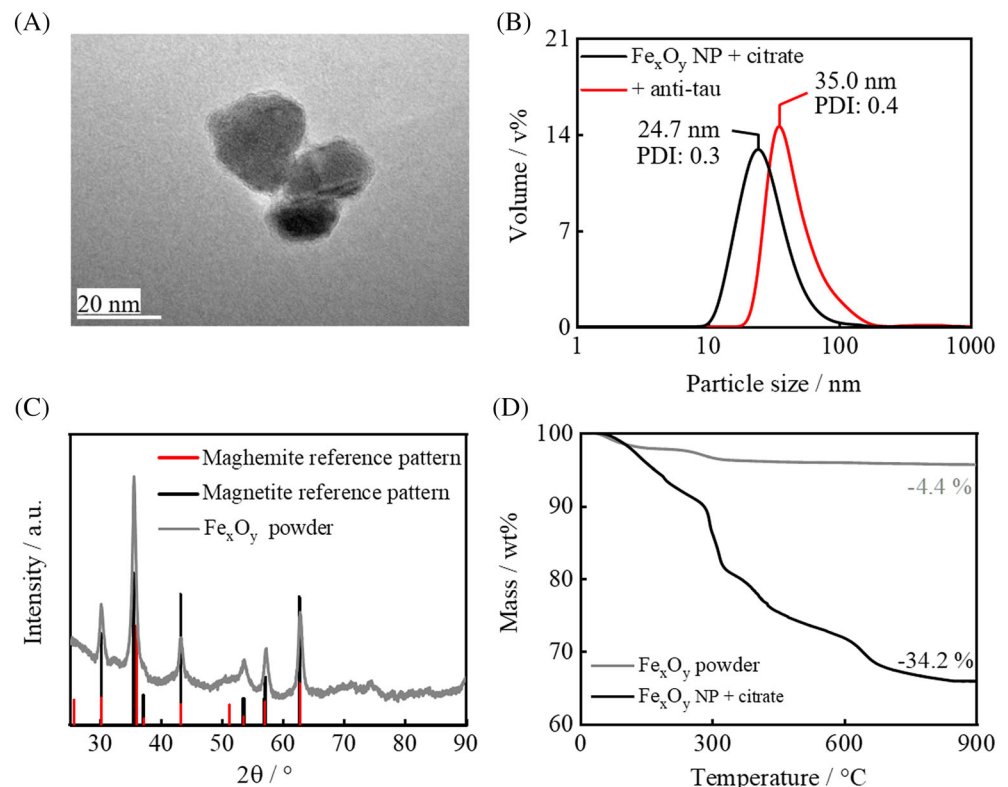


**FIGURE 2** A, Representative TEM image of the citrate-stabilized  $\text{Fe}_x\text{O}_y$  NPs, B, DLS results of  $\text{Fe}_x\text{O}_y$  NPs before and after antibody coupling with the respective median sizes and PDIs, C, XRD result of  $\text{Fe}_x\text{O}_y$  powder and a reference-pattern of magnetite and maghemite, D, thermogram of  $\text{Fe}_x\text{O}_y$  powder before and after dispersion with citric acid

From the XRD measurements together with the reference patterns (magnetite (98-015-8714) and maghemite (98-007-9196) from the Inorganic Crystal Structure Database (ICSD)), a crystalline mixed phase can be assigned to the  $\text{Fe}_x\text{O}_y$  powder (Figure 2D). Due to the wide signal width, a distinction between the magnetite and maghemite phases is not possible. The higher baseline in the range between  $25^\circ$  and  $35^\circ$  indicates amorphous contents. By applying the Debye-Scherrer equation to the highest intensity reflection at  $35.6^\circ$  with an FWHM of  $0.6^\circ$  and  $K_S$  of 0.9, a crystallite size of 12.7 nm was calculated. The deviation of approximately 12 nm from the hydrodynamic diameter implies that the prepared  $\text{Fe}_x\text{O}_y$  NPs consist of several crystallites.

Using EA, an increase in the amount of carbon by 9.1% and hydrogen by 1.2% on the  $\text{Fe}_x\text{O}_y$  NPs was determined after dispersion treatment with added citrate, which is fully attributed to citrate bound to the particle surface. Considering the molar masses of citrate and  $\text{Fe}_x\text{O}_y$  NPs, a mass fraction of 26.6 wt% represents the stabilizing citrate layer. Additionally, TGA measurements of the  $\text{Fe}_x\text{O}_y$  powder show a loss of 2.0 wt% within the ramp to  $150^\circ\text{C}$  as a result of excess water desorption (Figure 2C). Upon further heating, an additional weight loss of 2.4 wt% due to thermal decomposition of adsorbed organic compounds is observed. In contrast, the citrate stabilized particles

show a mass loss of 3.1 wt% due to evaporating water up to  $185^\circ\text{C}$ . A subsequent stepwise mass loss of altogether 31.1 wt% implies a multilayer system of citrate. The difference of the overall mass losses of 29.8 wt% (4.4 and 34.2 wt%) is the citrate contribution, which, considering the measurement accuracy, is in good agreement with the EA results.

### 3.2 | Synthesis of the gold nanoparticles

A spherical morphology of both the core and final Au NPs was revealed by TEM with the core colloids having an average particle size of approximately 12.0 and 38.2 nm, respectively (Figure 3A). The TEM image of the final nanoparticles proves their relatively high uniformity. The difference between the hydrodynamic diameter (Figure 3B) and the SAXS-derived diameter (calculated via  $R_{\text{max}}$  values, Figure 3C) is around 11.6 and 10.4 nm for the core colloid as well as 36.9 and 33.8 nm for the final colloid. This can be attributed to the measurement procedures, as for DLS measurements ligand effects exert a greater influence, whereas for SAXS only the crystalline core provides high electron contrast and contributes to the scattering. Furthermore, DLS measurements also indicate narrow size distributions and the SAXS results confirm spherical morphology as seen in the TEM images [36].

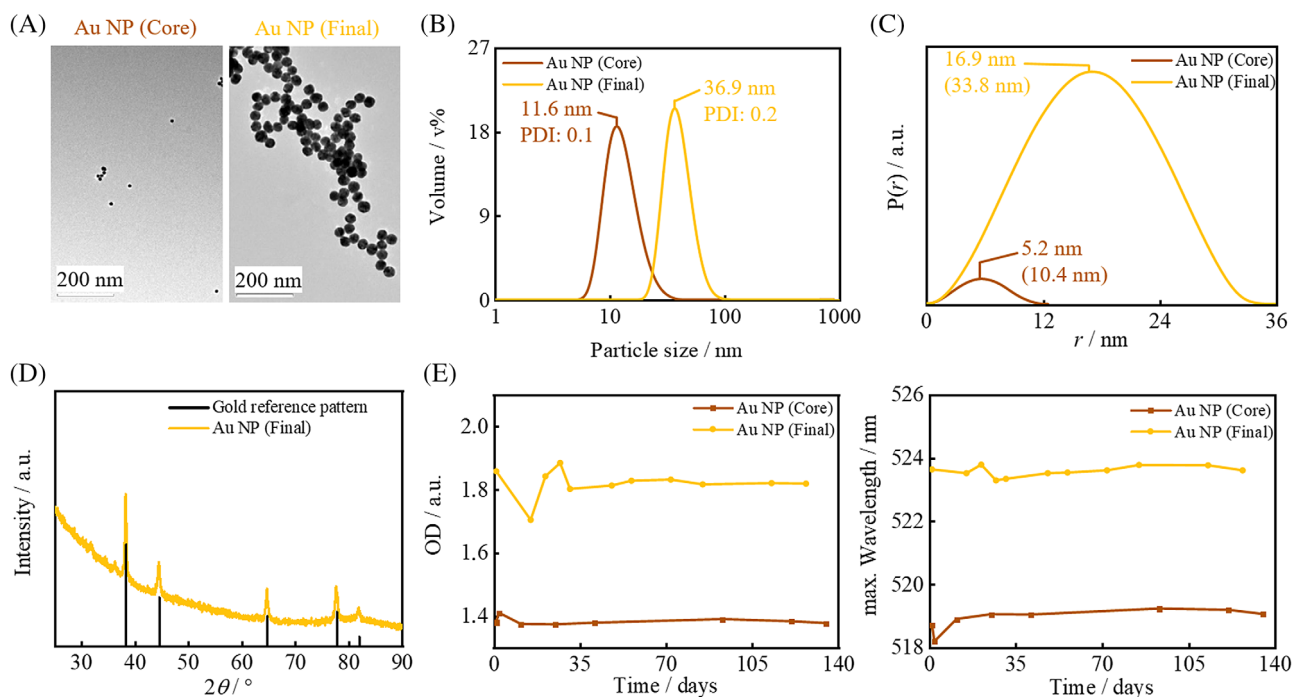


**FIGURE 3** A, TEM images, B, DLS measurements with the respective median sizes and PDIs, C, pair distance distribution functions with the respective  $R_{\text{max}}$  values and the corresponding diameters (in brackets), D, diffractogram with a gold reference-pattern, and E, plots of the maximum OD (left) obtained via UV/Vis measurements and of the respective wavelength (right) as a function of the ripening time of the synthesized Au NPs

XRD measurements show the representative diffractogram of a synthesized Au NP system, with both the core colloid and final colloid reflections shown at almost same position, matching the reference pattern (98-016-3723) and differing only in their width (Figure 3D). A crystallite size of 31.4 nm for the final colloid was calculated by applying the Debye–Scherrer equation to the highest intensity reflection at  $38.1^\circ$  with a FWHM of  $0.3^\circ$ . The difference of the colloid size calculated via XRD, SAXS, and TEM is attributed to an amorphous shell, which is also implied by the higher baseline in the range between  $25^\circ$  and  $35^\circ$ .

The long-term stability of the colloids was investigated by UV/Vis measurements using the progress of the OD and position of the according maxima for up to 140 days after synthesis (Figure 3E). After 10 days, the OD and the maximum position of the core colloids remain constant at 519.0 nm. After about 30 days, the final colloids reach the plateaus around 523.6 nm. In the following 100 days, all observed factors remain constant. For both colloid sizes, the occurrence of Ostwald ripening is the explaining factor for the initial variations [37].

### 3.3 | Hybrid complex assembly

After magnetic separation, a pinkish precipitate was obtained at the magnet-facing tube wall, implying the

presence of Au NPs bound to magnetic  $\text{Fe}_x\text{O}_y$  NPs (Figure 4A, left). After removing the unbound Au NPs, the solution still remained slightly pink (Figure 4A, right). Without tau protein or using another protein, a complete colorless solution was obtained after magnetic separation, showing the removal of all Au NPs (Figure 4A, right).

The TEM images show that next to all round and high-contrast Au NPs smaller  $\text{Fe}_x\text{O}_y$  NPs are located, which is attributed to the binding between the  $\text{Fe}_x\text{O}_y$ - and Au NPs via tau protein (Figure 4B, left). Furthermore, two large Au NPs are shown with smaller  $\text{Fe}_x\text{O}_y$  NPs in between which is either based on two different hybrid complexes with superposition of both complexes or on one big hybrid complex consisting of two Au NPs, as well as several  $\text{Fe}_x\text{O}_y$  NPs (Figure 4B, center). Different lattice fringes of crystalline  $\text{Fe}_x\text{O}_y$  and Au materials can be identified with a layer structure of the organic components DTNB and citrate enclosing both colloids (Figure 4B, right). In the Supporting Information, DLS spectra are presented in which an increase of the hydrodynamic diameter after each functionalization step can be observed (Figure S1C). Especially the modified diameter after addition of the functionalized  $\text{Fe}_x\text{O}_y$  NPs to the tau protein-coupled Au NPs indicates a successful complex formation as well.

To evaluate each functionalization step as well as the formation of the complete hybrid NP system, the zeta potentials of the individual precursors and the final

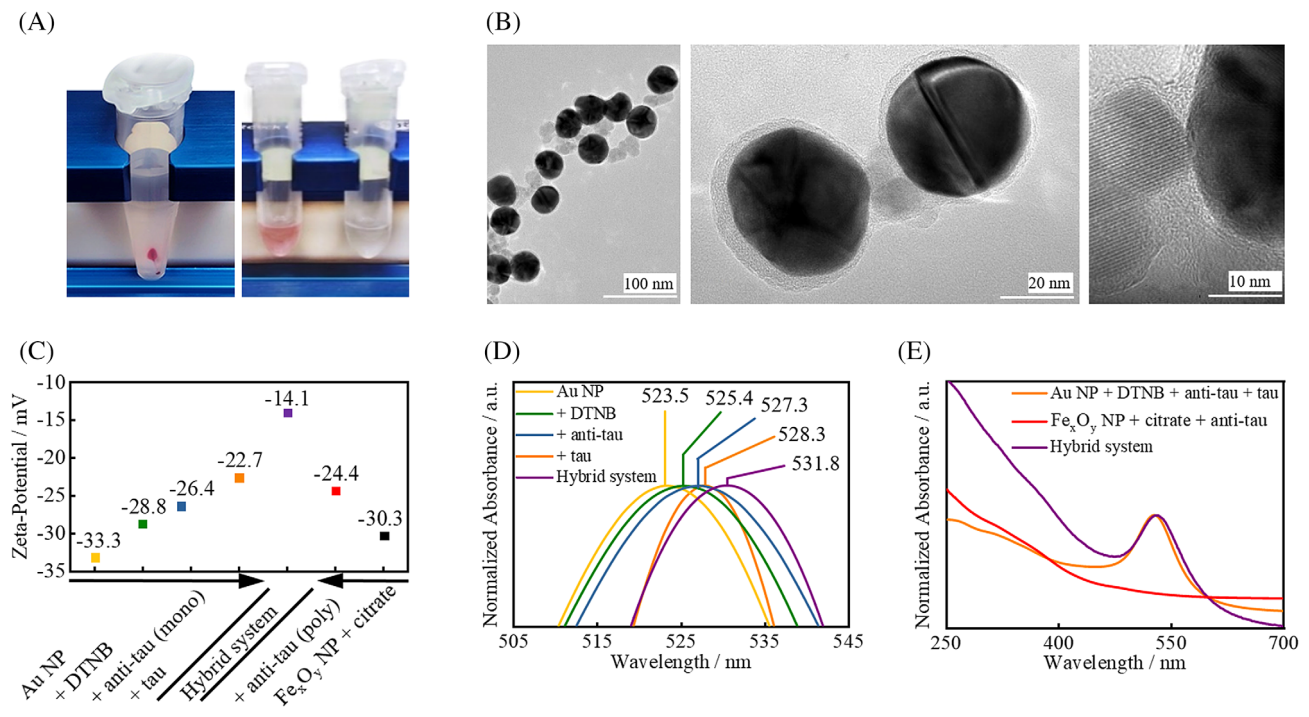


**FIGURE 4** A, Photographs of (left) magnetic separation of the hybrid complex, (right) resuspension after magnetic separation providing tau protein (magenta) and no or other proteins (colorless), B, TEM images of the synthesized hybrid NPs, C, zeta potential measurements of the NP systems for each process step, D, magnified UV/Vis spectra showing the absorption maxima of all individual Au NP systems, and E, normalized UV/Vis spectra of the synthesized hybrid NPs and their two colloidal precursors

complex were measured (Figure 4C). Due to the presence of citrate at the NP surface, both NP systems initially show highly negative zeta potentials. After each surface functionalization step of the respective NP system, a shielding of surface charges and a higher mass and thus bigger volume occurs, which leads to a reduced electrophoretic mobility, hence leading to a decrease in the absolute value of the zeta potentials. Since the binding of the functionalized Au NPs to the functionalized  $\text{Fe}_x\text{O}_y$  NPs combines two massive nanoparticulate structures via tau protein, the change of the zeta potential to  $-14.1$  mV is the most pronounced shift observed.

For further investigations, UV/Vis spectra were acquired after each functionalization step and normalized to the respective absorption maximum to unambiguously

characterize the shift of the corresponding wavelength (Figure 4D). The occurring red-shifts are based on an increased dielectric constant around the NP surface after a successful functionalization step [38]. Mixing the functionalized  $\text{Fe}_x\text{O}_y$  NPs with the tau protein-coupled Au NPs results in the largest shift by nearly 3.5 nm, possibly due to a major influence of the functionalized magnetic NPs. The full UV/Vis spectrum (250–700 nm) of the obtained hybrid system reflects both the Au-specific absorption maximum (around 525 nm) and the strong  $\text{Fe}_x\text{O}_y$ -specific increase of absorption from 450 nm toward lower wavelengths (Figure 4E). Since both the translocation of the maximum after each functionalization and the optical characteristics of both nanoparticulate components in the resulting UV/Vis spectrum can be detected, the

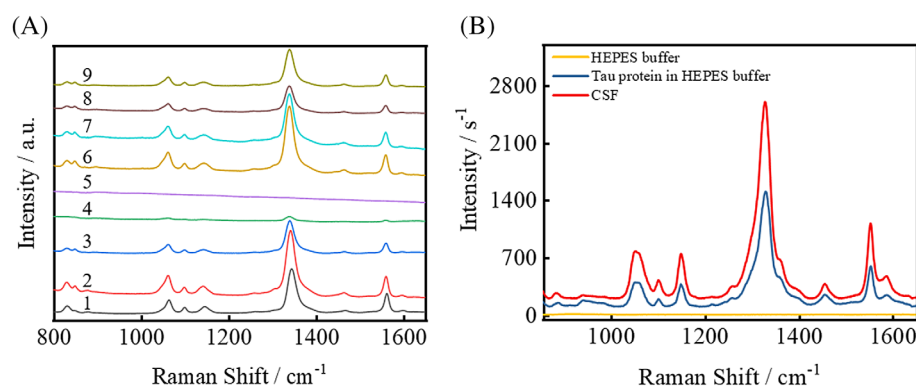


**FIGURE 5** A, Variations of the DTNB SERS signal after various preparation steps in the course of the Au NP functionalization: AuNP + DTNB (1), after incubation (2) and subsequent washing step (3), after anti-tau immobilization (4), incubation (5) and washing (6), after binding tau (7), incubation (8) and washing (9), B, SERS spectrum after hybrid NP synthesis in matrices with and without tau protein

**TABLE 1** Characterization concept containing measuring methods, resulting particle properties, and their overall importance for the establishment of SERS-based immunosensors

	Method	Measured properties	Importance
Primary particle synthesis	DLS	Agglomeration state	Required for quality control
	SAXS	Particle size, agglomeration state	Optional
	TEM	Particle size, morphology	Required for quality control
	TGA	Quantification of adsorbed organics	Optional if an established synthesis strategy is used; only useful for $\text{Fe}_x\text{O}_y$ NPs
	UV/Vis	Changes in particle size (e.g., fluctuations of absorption due to Ostwald ripening)	Optional; only relevant for Au NPs
	X-ray diffraction	Particle size, crystallinity	Recommended
	Zeta-potential	Surface charge based on the electrophoretic mobility	Required for quality control
Stepwise functionalization	DLS	Increase of hydrodynamic diameter; possible agglomeration	Optional if an established strategy is used
	TEM	Structural integrity of complex	Recommended
	UV/Vis	Absorption profile and shift	Required for quality control
	Zeta-Potential	Change of the electrophoretic mobility and surface charge	Required for quality control
Proof-of-concept	SERS	SERS-signal after magnetic separation	Crucial step



evaluation of the UV/Vis spectra also clearly indicates the successful formation of the hybrid NP system.

### 3.4 | Application of the hybrid complex

The washing procedures performed during the assembly of the hybrid complex always entail the risk of inducing precipitation of the Au NPs. Therefore, the number of washing steps should be kept to a minimum. The whole assembly process was monitored with Raman spectroscopy by evaluating the intensities of the Raman signals corresponding to the 5-thio-2-nitrobenzoic acid (TNB) molecule (Figure 5A,B), which is bound to the Au NP surface after the disulfide group of DTNB has dissociated in solution [39, 40]. Figure 5A shows the varying Raman intensities obtained during the preparation and washing steps while building up the Au NP moiety and the whole hybrid complex. It is obvious that excess and hence unbound antibody and tau protein quench the signal intensities in contrast to excess TNB. Due to their size, the protein as well as the antibody act as spacers which prevent the Au NPs from approximating each other to an extent required to achieve Raman signal enhancement. Additionally, after incubation with the antibody, only a broad background appears indicating a strong fluorescence, which completely suppresses the Raman spectrum. Washing the particles causes the signals to increase again as this treatment removes unbound substances and restores the associated ability to form plasmonic hotspots between the Au NPs.

To ensure that tau protein is the essential compound required to form one complex comprising Au- and  $\text{Fe}_x\text{O}_y$  NPs, a negative control was prepared and analyzed. Besides, as a proof of the applicability of the approach for analyzing real samples, measurements were carried out in CSF as the solvent (Figure 5B). It has been shown that in all cases where no tau protein has been added, that no TNB signals could be detected. This implies that no TNB-covered Au NPs remain in the sample solution and that only the presence of tau protein causes TNB signals to appear in the spectra proving the specificity and the selectivity of the complex for tau protein.

## 4 | CONCLUSIONS

In this study, a comprehensive characterization concept for a facile and defined formation of a SERS-based magnetic immunosensor is reported. Magnetic  $\text{Fe}_x\text{O}_y$  NPs with a citrate multilayer and a hydrodynamic diameter of about 24.7 nm were prepared and successfully conjugated with polyclonal anti-tau antibody. Spherical and highly uniform

colloidal Au NPs with a final size of approximately 36.0 nm as well as a narrow particle size distribution were obtained in a two-step preparation process followed by aging through Ostwald ripening for several weeks. Successful functionalization steps as well as the formation of the hybrid complex caused a decrease in the absolute value of the zeta potential, a larger hydrodynamic diameter as well as a step-wise red-shift of the absorption maximum. These results confirm the successful synthesis of a hybrid system having a defined structure as confirmed by the TEM images. As a proof-of-concept, the formation of the hybrid complex in tau protein-containing solutions enabled a detection of TNB spectra via SERS. Furthermore, the methods used can serve as a template for the characterization of magnetic SERS-based immunosensors and are summarized in Table 1.

The simplified preparation concept for a controlled formation for a SERS-active immunosensor greatly improves the applicability of this approach and allows a larger scale implementation. Furthermore, a quantification principle will be established utilizing the isotope dilution (ID) technique, which is mostly used in mass spectrometry, but which has also been shown to work excellently when combined with Raman spectroscopy [24, 25, 41–43]. Besides the advantages of having molecular specificity, accuracy and a high sensitivity during quantification, an ID-SERS approach also could provide SI-traceability of the measurement results when combined with well-characterized reference materials. In this way, reference measurement procedures can be implemented and also transferred to other biomarkers just by substituting the used antibodies.


### ACKNOWLEDGMENTS

The authors thank the Laboratory of Nano and Quantum Engineering (LNQE), Leibniz Universität Hannover, for the TEM instrument as well as B. Temel and D. Scholz for the excellent laboratory support. The work of this study is a part of the project 15HLT02, which was funded within the framework of the EMPIR. The EMPIR is jointly funded by the EMPIR participating countries within EURAMET and the European Union.

### CONFLICTS OF INTEREST

The authors declare no potential conflict of interest.

### ORCID

Georg Garnweitner  <https://orcid.org/0000-0002-7499-4947>

### REFERENCES

- [1] W. Muhammad, M. Haroon, M. Shah, M. A. Ullah, I. Haleem, *Nanoscale Rep.* **2018**, *1*, 1.

- [2] L. Mohammed, H. G. Gomma, D. Ragab, J. Zhu, *Particuology* **2017**, *30*, 1.
- [3] S. Stafford, R. Serrano Garcia, Y. Gun'ko, *Appl. Sci.* **2018**, *8*, 97.
- [4] N. Elahi, M. Kamali, M. H. Baghersad, *Talanta* **2018**, *184*, 537.
- [5] P. Zijlstra, P. M. R. Paulo, M. Orrit, *Nat. Nanotechnol.* **2012**, *7*, 379.
- [6] C. N. Kotanen, L. Martinez, R. Alvarez, J. W. Simecek, *Sens. Bio-Sens. Res.* **2016**, *8*, 20.
- [7] K. Zhang, C. Hao, Y. Huo, B. Man, C. Zhang, C. Yang, M. Liu, C. Chen, *Lasers Med. Sci.* **2019**, *34*, 1849.
- [8] S.-Y. Ding, J. Yi, J.-F. Li, B. Ren, D.-Y. Wu, R. Panneerselvam, Z.-Q. Tian, *Nat. Rev. Mater.* **2016**, *1*, 942.
- [9] L. Fabris, *ChemNanoMat* **2016**, *2*, 249.
- [10] S. L. Kleinman, R. R. Frontiera, A.-I. Henry, J. A. Dieringer, R. P. van Duyne, *Phys. Chem. Chem. Phys.* **2013**, *15*, 21.
- [11] H. Yang, L. Qu, A. N. Wimbrow, X. Jiang, Y. Sun, *Int. J. Food Microbiol.* **2007**, *118*, 132.
- [12] K. K. Singh, K. C. Sarma, E. Environ, *Nanotechnol. Monit. Manage.* **2016**, *6*, 206.
- [13] L. Xu, W. Yan, W. Ma, H. Kuang, X. Wu, L. Liu, Y. Zhao, L. Wang, C. Xu, *Adv. Mater.* **2015**, *27*, 1706.
- [14] H. Zhang, C. Fu, S. Wu, Y. Shen, C. Zhou, J. Neng, Y. Yi, Y. Jin, Y. Zhu, *Anal. Methods* **2019**, *11*, 783.
- [15] H. Zhang, Y. Yi, C. Zhou, G. Ying, X. Zhou, C. Fu, Y. Zhu, Y. Shen, *RSC Adv.* **2017**, *7*, 52782.
- [16] X. Fu, Z. Cheng, J. Yu, P. Choo, L. Chen, J. Choo, *Biosens. Bioelectron.* **2016**, *78*, 530.
- [17] H. Lai, F. Xu, L. Wang, J. Mater, *Science* **2018**, *53*, 8677.
- [18] G. Šimić, M. Babić Leko, S. Wray, C. Harrington, I. Delalle, N. Jovanov-Milošević, D. Bažadona, L. Buée, R. de Silva, G. Di Giovanni, C. Wischik, P. R. Hof, *Biomolecules* **2016**, *6*, 6.
- [19] H. Reiber, P. Lange, I. Zerr, *J. Alzheimers Dis. Parkinsonism* **2014**, *4*, 147.
- [20] A. Zengin, U. Tamer, T. Caykara, *Biomacromolecules* **2013**, *14*, 3001.
- [21] European Union. Regulation (EU) 2017/746 on in vitro diagnostic medical devices 2017.
- [22] Bureau International des poids et mesures, Le Système international d'unités (SI)—The International System of Units (SI). Draft 9th edn, Paris/Sè vres, France: BIPM <https://www.bipm.org/utis/en/pdf/si-revised-brochure/Draft-SI-Brochure-2018.pdf> 2019.
- [23] Bundesärztekammer, Richtlinie der Bundesärztekammer zur Qualitätssicherung laboratoriumsmedizinischer Untersuchungen (RiLiBÄK) **2014**.
- [24] S. Zakel, S. Wundrack, G. O'Connor, B. Güttler, R. Stosch, *J. Raman Spectrosc.* **2013**, *44*, 1246.
- [25] C. Frank, C. Brauckmann, M. Palos, C. G. Arsene, J. Neukammer, M. E. del Castillo Busto, S. Zakel, C. Swart, B. Güttler, R. Stosch, *Anal. Bioanal. Chem.* **2017**, *409*, 2341.
- [26] Bureau international des poids et mesures, Joint Committee for Guides in Metrology **2008**, 100.
- [27] A. Salmatoniadis, J. Hesselbach, G. Lilienkamp, T. Graumann, W. Daum, A. Kwade, G. Garnweitner, *Langmuir* **2018**, *34*, 6109.
- [28] I. M. Kolthoff, D. L. Leussing, T. S. Lee, *J. Am. Chem. Soc.* **1950**, *72*, 2173.
- [29] J. Taniuchi, H. Nakagawa, K. Okamoto. Process for production of colloidal gold and colloidal gold, WO2007142082 A1 **2007**.
- [30] B. R. Pauw, A. J. Smith, T. Snow, N. J. Terrill, A. F. Thünemann, *J. Appl. Cryst.* **2017**, *50*, 1800.
- [31] A. Bergmann, G. Fritz, O. Glatter, *J. Appl. Cryst.* **2000**, *33*, 1212.
- [32] American Society for Testing and Materials. E1840-96. Standard guide for raman shift standards for spectrometer calibration **2007**.
- [33] B. K. Sodipo, A. A. Aziz, *J. Magn. Magn. Mater.* **2016**, *416*, 275.
- [34] J. K. Armstrong, R. B. Wenby, H. J. Meiselman, T. C. Fisher, *Biophys. J.* **2004**, *87*, 4259.
- [35] A. Hawe, W. L. Hulse, W. Jiskoot, R. T. Forbes, *Pharm. Res.* **2011**, *28*, 2302.
- [36] H. Schnablegger and Y. Singh, *The SAXS Guide: Getting Acquainted with the Principles*, Anton Paar GmbH, Graz, AU **2017**.
- [37] N. T. K. Thanh, N. Maclean, S. Mahiddine, *Chem. Rev.* **2014**, *114*, 7610.
- [38] V. Amendola, M. Meneghetti, *J. Phys. Chem. C* **2009**, *113*, 4277.
- [39] M. Hesse, H. Meier, B. Zeeh. Spektroskopische Methoden in der organischen Chemie: 96 Tabellen, Thieme **1991**, pp. 336.
- [40] Z. Wang, S. Zong, H. Chen, H. Wu, Y. Cui, *Talanta* **2011**, *86*, 170.
- [41] C. Frank, O. Rienitz, R. Jährling, D. Schiel, S. Zakel, *Metallomics* **2012**, *4*, 1239.
- [42] F. R. Traube, S. Schiffers, K. Iwan, S. Kellner, F. Spada, M. Müller, T. Carell, *Nat. Protoc.* **2019**, *14*, 283.
- [43] J. K. Fallon, P. C. Smith, C. Q. Xia, M.-S. Kim, *Pharm. Res.* **2016**, *33*, 2280.

## SUPPORTING INFORMATION

Additional supporting information may be found online in the Supporting Information section at the end of this article.

**How to cite this article:** Maurer V, Frank C, Porsiel JC, Zellmer S, Garnweitner G, Stosch R. Step-by-step monitoring of a magnetic and SERS-active immunosensor assembly for purification and detection of tau protein. *J. Biophotonics*. 2020;13:e201960090. <https://doi.org/10.1002/jbio.201960090>